J. Fluid Mech. (2000), *vol.* 406, *pp.* 27–53. Printed in the United Kingdom

V-waves, bow shocks, and wakes in supercritical hydrostatic flow

By QINGFANG JIANG AND RONALD B. SMITH

Department of Geology and Geophysics, Yale University, New Haven, CT 06511, USA

(Received 5 March 1998 and in revised form 5 October 1999)

The structure of the bow shock, V-wave, and the related wave drag and wake in supercritical ambient flow are investigated for homogeneous hydrostatic single-layer flow with a free surface over an isolated two-dimensional (i.e. $h(x, y)$) obstacle. The two control parameters for this physical system are the ratio of obstacle height to fluid depth and the Froude number $F = U/\sqrt{gH}$. Based on theoretical analysis and numerical modelling, a steady-state regime diagram is constructed for supercritical flow. This study suggests that supercritical flow may have an upstream bow shock with a transition from the supercritical state to the subcritical state near the centreline, and a V-shock in the lee without a state transition. Unlike subcritical flow, neither a flank shock nor a normal lee shock is observed, due to the local supercritical environment. Both the bow shock and V-shock are dissipative and reduce the Bernoulli constant, but the vorticity generation is very weak in comparison with subcritical ambient flow. Thus, in supercritical flow, wakes are weak and eddy shedding is absent.

Formulae for V-wave shape and V-wave drag are given using linear theory. Both formulae compare well with numerical model runs for small obstacles.

These results can be applied to air flow over mountains, river hydraulics and coastal ocean currents with bottom topographies.

1. Introduction

Over the last five years, irrotational shallow water flow over an isolated two-dimensional (i.e. $h(x, y)$) bump has been well studied with respect to atmospheric applications (Schär & Smith 1993*a*, subsequently referred to herein as SS93*a*; Schär & Smith 1993*b*; Grubišić, Smith & Schär 1995; Smith & Smith 1995; Smith *et al.* 1997; Pan & Smith 1999). It has been demonstrated that a single-layer shallow water model can capture phenomena such as long wakes in the lee of obstacles, quasi-steady vortices, and vortex shedding, which have been observed in the atmosphere. With realistic parameters, a single-layer shallow water model as a representation of stratified air flow has even made some reasonable quantitative predictions such as vortex shedding period (Schär & Smith 1993*b*; Schär & Durran 1997) and wake length (Smith *et al.* 1997).

All these studies assumed that the environmental flow is subcritical. That is, the ambient flow speed is less than the long wave speed for gravity waves ($F_\infty < 1$). Therefore, if the ambient flow is accelerated by the terrain and becomes locally supercritical, it is still embedded in subcritical flow. In this situation, normal jumps

can form on the lee slope or flanks of the obstacles which dissipate energy, reduce the Bernoulli constant, and generate potential vorticity. It has been shown recently that the consideration of wavebreaking-induced potential vorticity generation is a useful approach to understanding the downstream effect of mountains. Further discussion of this issue can be found in Haynes & McIntyre (1987), Smith (1989), Schär (1993), and SS93*a*.

In this study, we extend previous work into the supercritical range. Our primary interests are the linear wave response, wave drag, finite-amplitude wave structure, and the wavebreaking mechanism for vorticity generation. In practice, we limit our attention to Froude numbers in the range $1.2 < F < 3$.

One motivation for this work comes from our study of multi-layer models of atmospheric flow. While the real atmosphere is often continuously stratified, it may occasionally have a layered structure due to inversions. It is quite common that as air flows over the cold sea surface, a shallow marine atmospheric boundary layer (MABL) may develop underneath a low-level inversion. To some extent, these inversions decouple the MABL from the free atmosphere (i.e. the air above the MABL), which allows us to treat the MABL as a single-layer flow with an appropriately reduced gravity.

For instance, the shallow marine atmospheric boundary layer under a low-level inversion along the California coast has been treated as a supercritical hydrostatic flow with a side wall by Samelson (1992) and Samelson & Lentz (1994). As an estimation, given a depth of the MABL of around 300 m, the reduced gravity can be expressed as $g' = g\theta'/\theta$ where θ is the potential temperature and θ' is the potential temperature difference across the inversion. Given $\theta' = 3.0\,\mathrm{K}$ and $\theta = 300\,\mathrm{K}$, the hydrostatic surface wave speed is about $5.5\,\mathrm{m\,s^{-1}}$. A common wind speed such as $10\,\mathrm{m\,s^{-1}}$ will give Froude number $F = 1.8$. Their modelling sucessfully captured some of the features observed in the CODE-2 field experiment. Another example, a striking long dark band extending from the island of Jan Mayen appearing on a satellite image (Gjevik & Marthinsen 1978), was later identified as supercritical wave (Baines 1995). The estimated Froude number for this case was 1.6.

Supercritical dynamics can also be found in river flow and coastal currents. For example, a 2 m deep river gives a hydrostatic wave speed of $4.4\,\mathrm{m\,s^{-1}}$, which can be exceeded by a river flow in flood. Even ocean currents can be locally supercritical in coastal seas due to ocean thermoclines. For instance, a layered structure can be observed in Long Island Sound (Wilson 1976). The reduced gravity can be estimated as $g' = g\rho'/\rho$ where ρ is the current density and ρ' is the density difference across the thermoclines. Given $\rho'/\rho = 0.005$, flow depth $H = 10\,\mathrm{m}$, the resulting wave speed is $0.7\,\mathrm{m\,s^{-1}}$, which can be well below tidal flow speed ($\sim$1–3 $\mathrm{m\,s^{-1}}$).

A brief discussion of the qualitative features of supercritical shallow water flow over a two-dimensional bump was given in Baines (1995), mainly based on the comparison with compressible aerodynamics. Much earlier, supercritical flow over one-dimensional topography (i.e. $h(x)$) was experimentally and theoretically explored (Long 1954, 1970; Houghton & Kasahara 1968). A recent analysis of one-dimensional hydraulics is given by Broad (1997) and Baines (1995). The hydrostatic wave drag has been studied by Tuck (1966) with a ship-like slender body on the free surface.

The outline of this paper is as follows: § 2 contains some linear theory predictions. In § 3, a regime diagram is constructed based on the theoretical considerations and numerical simulations. Supercritical wave drag is discussed in § 4. In § 5, the structure of the bow shock and V-shock, and vorticity generation are analysed. This study is summarized in § 6.

2. Linear theory of V-waves

2.1. *Shallow water equations*

In the inviscid and hydrostatic limit, the governing equations for single-layer shallow water flow with a free surface are as follows (Stoker 1957, p. 32):

$$\frac{\mathrm{D}u}{\mathrm{D}t} + g'(h+H)_x = 0, \tag{1}$$

$$\frac{\mathrm{D}v}{\mathrm{D}t} + g'(h+H)_y = 0, \tag{2}$$

$$\frac{\mathrm{D}H}{\mathrm{D}t} + H(u_x + v_y) = 0, \tag{3}$$

where (u, v) is the horizontal velocity field, H is the flow depth, h is the bottom elevation, and g' is the reduced gravity. System (1)–(3) is known as Airy's theory, long wave theory, or shallow water theory.

It should be emphasized that while shallow water theory can greatly simplify problems, its limitation is also well known. Equations (1)–(3) are only valid in the limit of

$$(H/L)^2 \ll 1 \tag{4}$$

where L is the horizontal scale. Otherwise the dispersion ignored in system (1)–(3) can be important. If the horizontal scale L chosen as the length scale of perturbation source satisfies (4), the shallow water assumption may often be valid. However, as is well known, nonlinear processes can generate higher-order harmonic or shorter waves, which bring in smaller horizontal scales. Thus, a further justification for using the hydrostatic assumption for nonlinear waves will be required (§ 3).

2.2. *Linear solution*

For a steady-state flow with bottom elevation $h(x, y)$, the linearized equations can be written as

$$U_\infty u_x = -g'\eta_x, \tag{5}$$

$$U_\infty v_x = -g'\eta_y, \tag{6}$$

$$U_\infty \eta_x + H_\infty(u_x + v_y) = U_\infty h_x, \tag{7}$$

where H_∞ is the reference flow depth, U_∞ is the reference velocity, u and v are the perturbation velocities, which satisfy $|u, v| \ll U_\infty$, and η is the departure of the free surface elevation from the reference state, which satisfies $\eta \ll H_\infty$.

Combining (5), (6), and (7) to eliminate u and v, gives

$$F_\infty^2(h-\eta)_{xx} = -\nabla^2\eta \tag{8}$$

For supercritical flow, this is a hyperbolic equation. The solution can be obtained by the Green's function method (see Appendix A):

$$\eta(x,y) = \frac{F_\infty^2}{2\sqrt{F_\infty^2-1}}\frac{\partial}{\partial x}\left\{\int_{-\infty}^{y} h(x-\sqrt{F_\infty^2-1}(y-y_0), y_0)\,\mathrm{d}y_0 + \int_{y}^{\infty} h(x+\sqrt{F_\infty^2-1}(y-y_0), y_0)\,\mathrm{d}y_0\right\}. \tag{9}$$

Equation (9) corrects a recent solution given by Baines (1995) which has a similar form

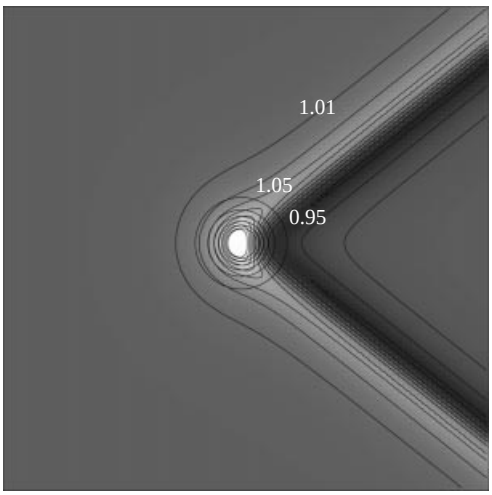

FIGURE 1. Linear solution to the steady-state single-layer supercritical flow given by (12). Free surface height is contoured for $M = 0.1$, $F_\infty = 1.6$.

to (9) except the integration interval is $(-\infty, \infty)$ (Baines, personal communication). Baines' solution satisfies (8) only if $h_{xx} = 0$.

The idealized obstacle used in this study is a circular topography described by two parameters: the maximum mountain height h_m and half-width a (Wurtele 1957 and Smith 1980):

$$h(x, y) = \frac{h_m}{[1 + (x/a)^2 + (y/a)^2]^{3/2}} \tag{10}$$

or in non-dimensional form

$$h(x, y) = \frac{M}{[1 + x^2 + y^2]^{3/2}}, \tag{11}$$

where $M = h_m/H_\infty$, (x, y) is non-dimensionalized with a. From (9) and (11), we obtain

$$\begin{aligned}
\eta(x, y) = &-\frac{AM}{B}\left\{\frac{Ax - By}{[1 + (Ax - By)^2]^2} + \frac{Ax + By}{[1 + (Ax + By)^2]^2}\right\} \\
&-\frac{Mx}{2B(1 + R^2)^{3/2}}\left\{\frac{Bx - Ay}{1 + (Ax + By)^2} + \frac{Bx + Ay}{1 + (Ax - By)^2}\right\} \\
&+\frac{M}{2(1 + R^2)^{1/2}}\left\{\frac{1}{(1 + (Ax + By)^2)^2} + \frac{1}{(1 + (Ax - By)^2)^2}\right\} \\
&+\frac{M}{2B(1 + R^2)^{1/2}}\left\{\frac{(Ax + By)(-ABx + B^2y + 2A^2y)}{[1 + (Ax + By)^2]^2}\right. \\
&\left.+\frac{(By - Ax)(ABx + B^2y + 2A^2y)}{[1 + (Ax - By)^2]^2}\right\},
\end{aligned} \tag{12}$$

where $A = \sin\alpha_0$, $B = \cos\alpha_0$, and $\alpha_0 = \arcsin(F_\infty^{-1})$ is the Mach angle. For $M = 0.1$, $F_\infty = 1.6$, the solution (12) is contoured in figure 1.

Note that as $(x, y) \to \infty$ with $x > 0$, some of the terms in (12) will vanish, and we are left with stationary waves extending to infinity at the Mach angle from the

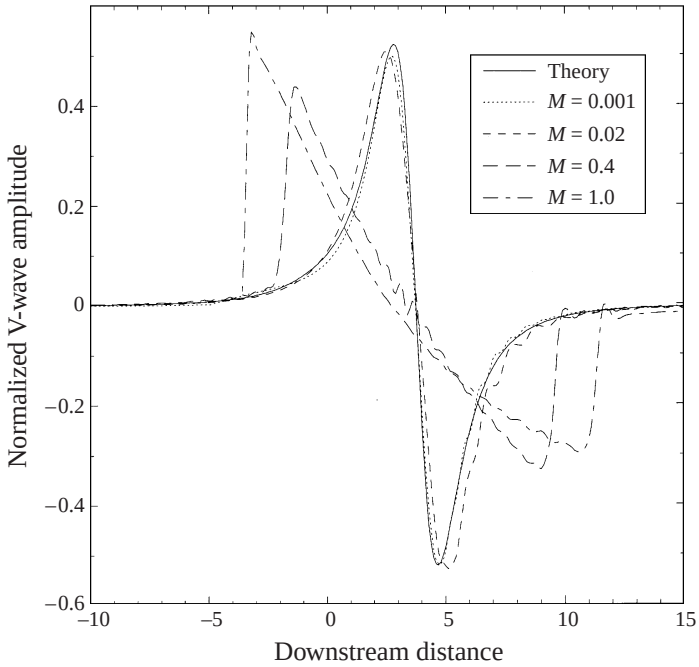

FIGURE 2. Linear solutions for free surface height compared to a numerical model. Normalized (by h_m) V-wave amplitude versus downstream distance x for fixed $y = 5$ and different mountain heights: $M = 0.001$, 0.02, 0.4, 1.0. The solid curve is the linear solution (12).

upstream flow direction. For a symmetric topography, there are two separated beams, which are symmetric around the centreline in the shape of a V. For simplicity, we call it a V-wave.

Far downstream of the bump, an asymptotic solution can be expressed in local coordinates. Let $x = x_L - A\xi$ and $y = y_L + B\xi$ be substituted into terms with $Ax - By$ in the denominator, and $x = x_R - A\varsigma$ and $y = y_R + B\varsigma$ be substituted into terms with $Ax + By$, where (x_L, y_L), (x_R, y_R) are points projected on the Mach lines emanating from the origin. The local coordinates ξ, ς are the distances from the point (x, y) to the V-wave axes (x_L, y_L) and (x_R, y_R), respectively. As $x \to \infty$, the asymptotic form of (12) is

$$\eta(\xi, \varsigma) = \frac{2M}{\sqrt{F_\infty^2 - 1}} \left[\frac{\xi}{(1+\xi^2)^2} + \frac{\varsigma}{(1+\varsigma^2)^2} \right]. \tag{13}$$

Solutions (12) and (13) can be used to test the numerical model described in § 3. In figure 2, the linear solution is compared to numerical runs for $F_\infty = 1.6$, and various mountain heights. When the hill is small ($M \ll 1$), the linear solution agrees well with numerical runs. As the hill height increases, the V-wave close to the topography gradually becomes steeper due to nonlinearity. The leading edge steepens, moves forward and becomes a bow shock, while the trailing edge steepens, moves downstream, and becomes an oblique shock (figure 2). In compressible gas dynamics, this pattern is called an N wave (e.g. Whitham 1974, p. 48).

Using a similar technique, we can obtain the solution for an elliptical hill of the form

$$h(x, y) = \frac{h_m}{[1 + (x/a)^2 + (y/b)^2]^{3/2}}. \tag{14}$$

The far-field asymptotic solution for an elliptical hill becomes

$$\eta(\xi,\varsigma)=\frac{2Mc}{\sqrt{F_\infty^2-1}}\left[\frac{\xi}{(1+c^2\xi^2)^2}+\frac{\varsigma}{(1+c^2\varsigma^2)^2}\right], \tag{15}$$

where $c=A^2/a+B^2/b$. The full solution can be seen in Appendix A.

3. Nonlinear simulations

3.1. *The SWM model*

3.1.1. *Modelling steepened waves as discontinuities*

Even if condition (4) is satisfied, the slope of the steepened shallow water wave can be so large that the hydrostatic assumption becomes locally invalid. One approach to this problem is to expand the full non-hydrostatic (Euler) equation in two small parameters (i.e. A/H and H/L, where A is the nonlinear wave amplitude), and keep the leading terms to different orders. Depending on the details of the procedure, this approach gives a variety of equations governing weakly nonlinear and dispersive waves such as the Boussinesq equation (Whitham 1974; Wu 1987), the KdV equation (Korteweg & Vries 1895; Peregrine 1968; and Bona, Prichard & Scott 1981), the intermediate-long-wave (ILW) equation (Joseph 1977; Kubota, Ko & Dobbs 1978), and the Benjamin-Ono (B-O) equation (Whitham 1974). An advantage of this type of formulations is that analytical solutions, such as the famous solitary wave solution, can be derived. It also allows transcritical flow ($F_\infty\sim 1$) to be treated analytically.

Another approach to the nonlinear wave steepening and wavebreaking issue is hydraulic theory. The wavebreaking region is treated as a discontinuity governed by mass and momentum conservation, i.e. Airy's theory. As pointed out by Mei (1989), this approach is probably inadequate for the prediction of initial wavebreaking, but relevant to the events after breaking. This approach can even be justified for dissipative undular bores. The speed and amplitude of propagating undular bores observed in laboratory channels can be well described using hydraulic theory (e.g. Binnie & Orkney 1955). Also, as observed in the laboratory, the amplitude of the bore undulation decreases with distance from the leading edge and, provided there is no other forcing, it eventually reaches a uniform equilibrium state. Instead of describing the detailed structure of undular bores, hydraulic theory imposes a restriction on the downstream equilibrium state using conservation laws. In summary, hydraulic theory may not be appropriate to describe the precise pre-wavebreaking processes or the detailed structure in the wavebreaking region: however, it can describe the flow downstream of the wavebreaking region. Compared with the weakly nonlinear approach, the advantage of hydraulic theory is that a fully nonlinear problem can be treated in a simple analytical way (Stoker 1957).

3.1.2. *Modelling the internal dissipation in a hydraulic jump*

The shallow water model (SWM) used here was developed by Schär & Smith (1993*a*, *b*). The governing equations are the full shallow water equations (1)–(3) in non-dimensional form,

$$\frac{\mathrm{D}\boldsymbol{v}}{\mathrm{D}t}+\nabla(h+H)=\frac{1}{Re}\nabla^2\boldsymbol{v}, \tag{16}$$

$$\frac{\mathrm{D}H}{\mathrm{D}t}+H\nabla\cdot\boldsymbol{v}=0, \tag{17}$$

where $\boldsymbol{v} = (u, v)$ is the velocity vector, and $Re = va/U_\infty$ is the Reynolds number based on the mountain width. The following scales have been used: the half-width of obstacle a for horizontal length scale, the upstream depth H_∞ for the vertical scale, upstream gravity wave speed $\sqrt{g'H_\infty}$ for the horizontal velocity scale and $a/\sqrt{g'H_\infty}$ for the time scale.

Equations (16)–(17) can be written in flux form (SS93*a*),

$$\frac{\partial \boldsymbol{V}}{\partial t} + \nabla \cdot (\boldsymbol{v}\boldsymbol{V}) + H\nabla(h + H) = \frac{1}{Re}\nabla \cdot (H\nabla \boldsymbol{v}), \tag{18}$$

where $\boldsymbol{V} = H\boldsymbol{v}$ is the vertically integrated momentum, or momentum flux. The velocity field is derived from the diagnostic relation $\boldsymbol{v} = \boldsymbol{V}/H$. A critical issue in the modelling of hydraulic jumps is the simulation of the internal dissipation which occurs in shocks. There are two types of dissipation in the SWM: explicit viscosity and numerical viscosity. For large Reynolds number flow, such as flow in the ocean and the atmosphere, we arbitrarily use a small explicit viscosity ($Re = 2000$ in our simulations) to slightly smooth the flow field. Hence, the dominant dissipative effect in our simulations is numerical.

In the model, equations (17)–(18) are integrated on a rectangular grid. The conservation of vertically integrated momentum and mass is strictly imposed at each time step. Although systems (16)–(17) and (17)–(18) are equivalent, this equivalence breaks down near hydraulic jump region in the SWM, where the free surface is so steep that the flow velocity derived from numerical integration of (17)–(18) cannot satisfy the momentum equations (16)–(17). The numerical viscosity plays a role in equation (16) such as an additional dissipative force (SS93*a*).

It should be pointed out that because we do not intend to resolve the details in a shock, it is not necessary to probe the role of the numerical viscosity at grid points within the shock. For our purposes, the most important issue is to determine the 'right' post-shock flow state, which is guaranteed by the momentum/mass conservation law.

An alternative to this approach is to decrease the Reynolds number sufficiently so that the explicit viscosity will dominate the numerical viscosity. Because the diffusion term in equation (18) is in flux form, it does not destroy any momentum, and the mass/momentum conservation law still holds across any hydraulic jump. It has been shown in previous studies that the SWM predictions of general flow features and potential vorticity generation were insensitive to Reynolds number (SS93*a* and Smith & Smith 1995). Further test runs in this study confirm that over a large range of Reynolds numbers, although the jump has a tendency to become broader with increasing viscosity, the end state only changes slightly. The numerical details of this SWM can be found in SS93*a*, and Schär & Smolarkiewicz (1996).

3.2. *Regime diagram*

A large domain size ($-40 < x < 60$, $-60 < y < 60$) is chosen to capture the far-field structure of the bow shock and V-wave, with a spatial resolution $\mathrm{D}X = \mathrm{D}Y = 0.2$, and a temporal resolution $\mathrm{D}T = 0.025$. A free advection boundary condition is used along the lateral boundaries. The variables uH, vH, H, h are represented on a 500×600 grid.

A circular topography (10) sits in the middle domain. A high topography is allowed to pierce through the interface. When piercing occurs, the region inside the interception curve is treated as a 'dry region', i.e. zero depth and zero momentum. Test runs show that the model is numerically stable if the Courant–Friedrich–Levy criterion is satisfied. The integrations are carried out until a steady state is reached.

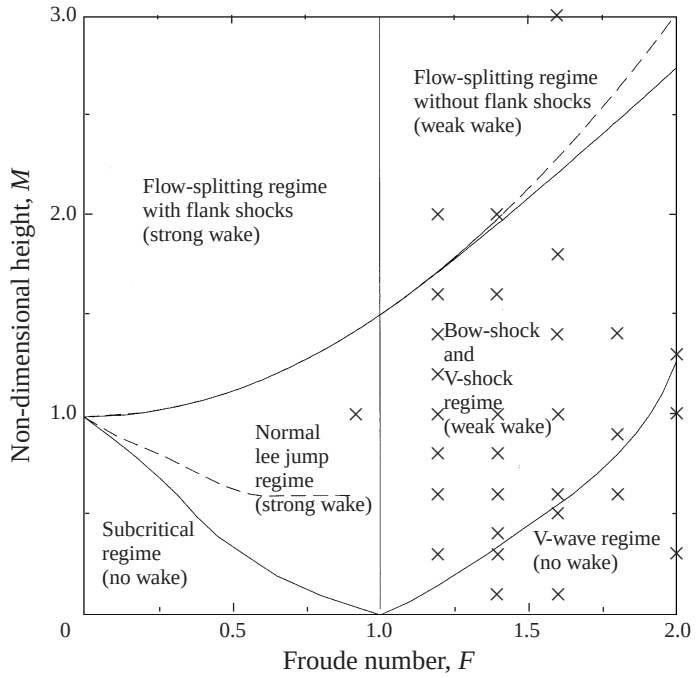

FIGURE 3. Steady-state regime diagram for shallow water flow past a two-dimensional bump, with two control parameters: upstream Froude number and dimensionless mountain height. The subcritical part is taken from SS93*a*. Some aspects of this diagram have been described by Baines (1995, p. 85). The dashed line in the upper right neglects Bernoulli loss across the bow shock (19). The solid upper line is (20). The symbols '×' indicate numerical runs.

The steady-state solutions for hydrostatic flow past an isolated two-dimensional bump in the absence of bottom friction are determined by two non-dimensional parameters: the ambient Froude number F_∞ and the dimensionless mountain height M. Therefore the qualitative features of these solutions can be mapped onto a $F_\infty \times M$ regime diagram.

A regime diagram for subcritical flow ($F_\infty < 1$) has been constructed by SS93*a*. In their diagram, the subcritical flow was divided into three regimes: subcritical fore-aft symmetric flow, locally supercritical flow with normal jump on the lee side, and flow splitting with flank jumps and reversed flow. The second regime was further divided into two subregimes: weak jump with a long straight wake and strong jump with wake eddies. Here we extend their diagram to include supercritical flow. Some speculations about this diagram have been discussed by Baines (1995, p. 85).

The complete regime diagram is shown as figure 3. The supercritical region has been divided into three regimes based on a large number of numerical simulations with differing flow parameters ($1.2 < F_\infty < 2.0$; $0 < M < 3$):

V-*wave regime.* In this regime, which corresponds to flow over a small hill, the flow is purely supercritical over the whole domain. There is no bow shock in front of the topography. Contrary to the fore-aft symmetric structure of subcritical flow, there is a long non-dispersive V-wave on the lee side (figure 4*a*). The flow in this regime can be qualitatively described by the linear solution derived in § 2. The flow across the trailing V-wave decelerates first and then accelerates while passing the trailing part. On the lee slope of the hill, there is a fast flow region corresponding to a depression

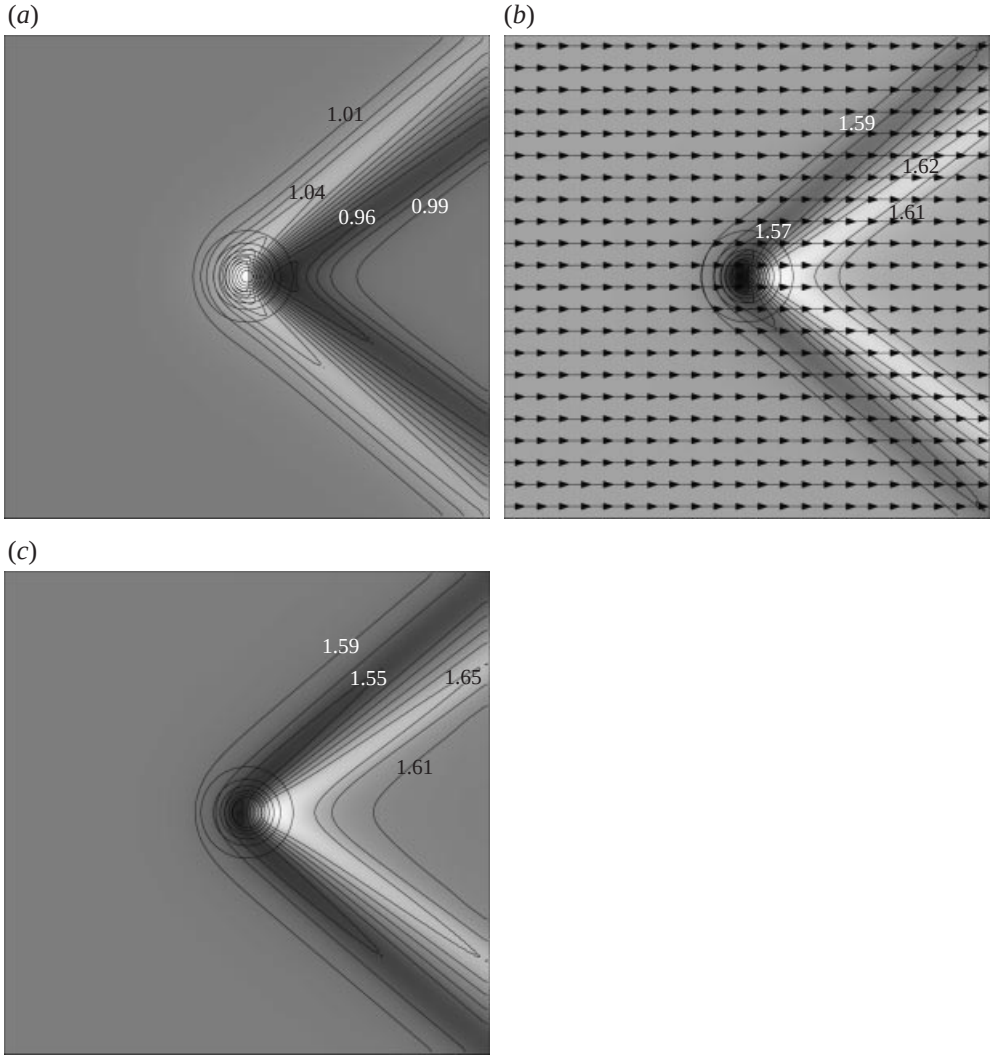

FIGURE 4. Steady-state solutions for $M = 0.1, F_\infty = 1.6$ (V-wave regime): (*a*) free surface height contours, (*b*) wind speed contours and wind vectors, (*c*) local Froude number contours.

of the free surface (figure 4*a*) and a strong convergence towards the centre due to the lateral pressure gradient force.

Bow-wave and V-wave regime. This regime corresponds to supercritical flow over a higher hill. There is a stationary bow shock present in front of the topography (i.e. bow shock). Near the centreline, flow across the jump becomes subcritical, and is deflected away from the centreline. After the bow shock, the subcritical flow is smoothly accelerated back into a supercritical state by the pressure gradient force accompanied by convergence towards the centreline. The supercritical flow experiences an oblique jump at the trailing edge of the V-wave beams, and is decelerated again. There is no state transition found across the trailing V-wave, i.e. the flow is supercritical before and after the jump. Near the centreline, in the lee side of the obstacle, there is fast flow with a very thin depth and a large local Froude number (figure 5).

Vorticity generation is found both in front of the topography because of the bow shock dissipation and on the lee side due to the V-wave dissipation. However, the

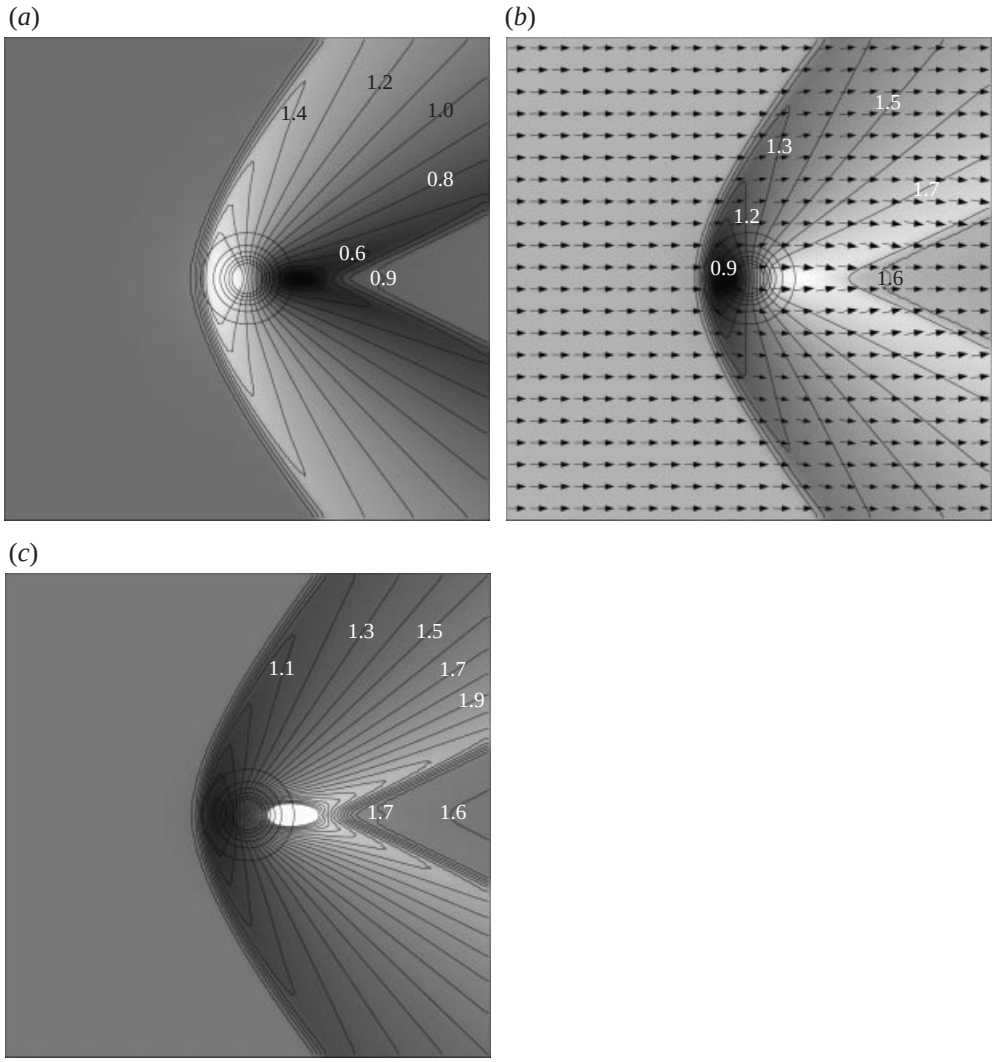

FIGURE 5. As in figure 4 but for $M = 1.0, F_\infty = 1.6$ (bow-wave and V-wave regime).

vorticity is much smaller (usually by a factor of 100) than the vorticity generated by the normal lee jumps or flank jumps in subcritical ambient flow (see § 5.4).

Flow splitting regime. In this regime, the topography is so high that the flow is pierced by the hill (figure 6). As in subcritical flow, there is a stagnation point on the front slope. However, the most striking features of subcritical flow in the flow splitting regime, namely flank jumps with strong vorticity generation and reversed flow on the lee side, never appear in supercritical flow. This is so, even though the flow is highly supercritical near the hill where the depth goes to zero. It implies that, while a (normal) jump with state transition is necessary when supercritical flow is surrounded with subcritical flow, when highly supercritical ($F_\infty \gg 1$) flow is surrounded with supercritical flow, a jump is not necessary.

There is a strong bow shock present in front of the obstacle, and a V-wave shock on the lee side (figure 6). The lee slope, which featured a fast flow region in the other two regimes, now becomes dry.

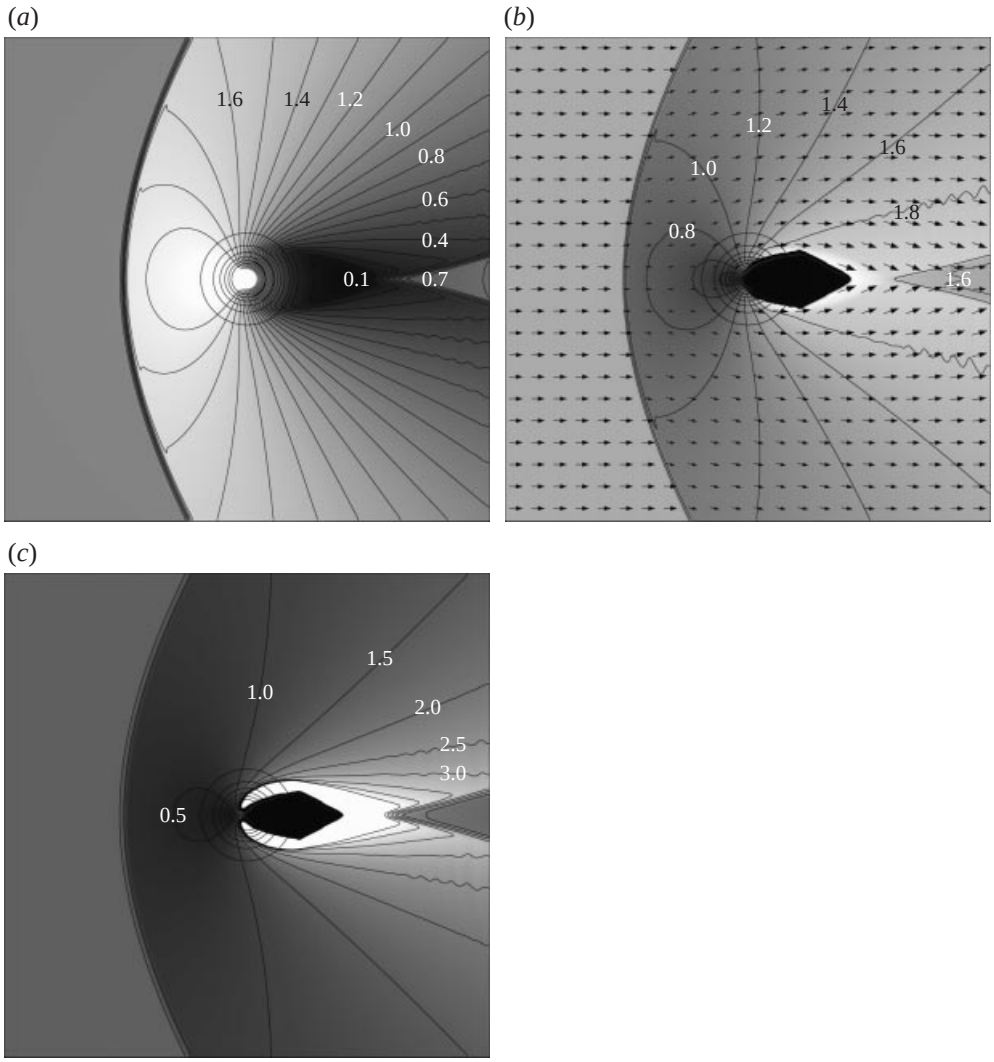

FIGURE 6. As in figure 5 but for $F_\infty = 1.6$, $M = 2.5$ (flow splitting regime). The heavy angular contour downstream of the peak represents the dry region where the velocity has arbitrarily been set to zero.

The boundary between the flow splitting regime and bow shock regime can be theoretically determined. For subcritical flow, this regime boundary is determined by applying the steady-state Bernoulli law along the centreline (SS93*a*). Considering that the stagnation point must appear first on the peak, the critical curve can be obtained by letting $u = H = 0$ at the peak of the topography:

$$M = 1 + \tfrac{1}{2}F_\infty^2. \tag{19}$$

For a supercritical flow, flow along the centreline may experience an upstream jump first, which reduces the Bernoulli constant, so that flow splitting will occur for a slightly lower hill. Applying the normal jump condition to the flow along the centreline, the Bernoulli loss can be expressed in terms of upstream variables. Along the centreline, the Bernoulli function should be constant between the upstream jump and the peak

(see § 5). Again assuming that the stagnation point first appears on the peak, we obtain the modified critical curve for supercritical flow (Baines 1995, p. 87):

$$M = \tfrac{1}{2}\sqrt{1+8F_\infty^2} - \tfrac{1}{4} + \frac{1+\sqrt{1+8F_\infty^2}}{16F_\infty^2}. \tag{20}$$

Equation (20) is plotted on figure 3, and (19) is the dashed curve for reference. The two curves do not differ significantly over the range shown.

4. V-wave drag

4.1. *Linear V-wave drag*

The presence of a V-wave introduces fore-aft depth and pressure asymmetry above the topography, giving a net V-wave drag on the topography, even in the absence of any nonlinearity or shocks. The mountain drag D induced by the linear V-wave for shallow water flow can be expressed as (Smith 1979)

$$D = \int\int_{-\infty}^{\infty} P' h_x \,\mathrm{d}x\,\mathrm{d}y \tag{21}$$

where

$$P' = \rho g \eta \tag{22}$$

is the hydrostatic pressure perturbation, and η is the departure in free surface height governed by equation (8). Applying a double Fourier transform, drag D can be expressed as

$$D = \mathrm{i}\rho g \int\int_{-\infty}^{\infty} 4\pi^2 \hat{h}(-k,l) k \hat{\eta}\,\mathrm{d}k\,\mathrm{d}l \tag{23}$$

where $\hat{h}(k,l)$ is the Fourier transform of the topography.

For the topography (11), $\hat{h}(k,l)$ can be expressed in a closed form (SS93*a*):

$$\hat{h}(k,l) = \frac{M}{2\pi}\mathrm{e}^{-K} \tag{24}$$

where $K = \sqrt{k^2+l^2}$. If the integral (23) is evaluated directly, we obtain $D = 0$, because the linear solution includes two pairs of V-wave beams, a pair on the lee side and on the upstream side. The upstream pair is unphysical, as no small-amplitude waves can propagate upstream in supercritical flow. To eliminate the effect of the 'upstream V-wave', we introduce small explicit viscosity into the equations (Queney 1947).

Equation (8) with viscosity becomes

$$F_\infty^2 (h-\eta)_{xx} = -\nabla^2 \eta + \nu \nabla^2 (h-\eta)_x \tag{25}$$

where $F_\infty^2 = U_\infty^2/gH_\infty$ is the upstream Froude number, and $\nu = 1/Re$.

Applying a double Fourier transform, the solution can be expressed as

$$\eta(x,y) = \int\int_{-\infty}^{\infty} \hat{\eta}(k,l)\mathrm{e}^{\mathrm{i}(kx+ly)}\,\mathrm{d}k\,\mathrm{d}l \tag{26}$$

where

$$\hat{\eta}(k,l) = \frac{[F_\infty^2 - \mathrm{i}\nu k^3/(k^2+l^2)]\hat{h}(k,l)}{F_\infty^2 - (k^2+l^2)k^{-2} - \mathrm{i}\nu k^3/(k^2+l^2)}. \tag{27}$$

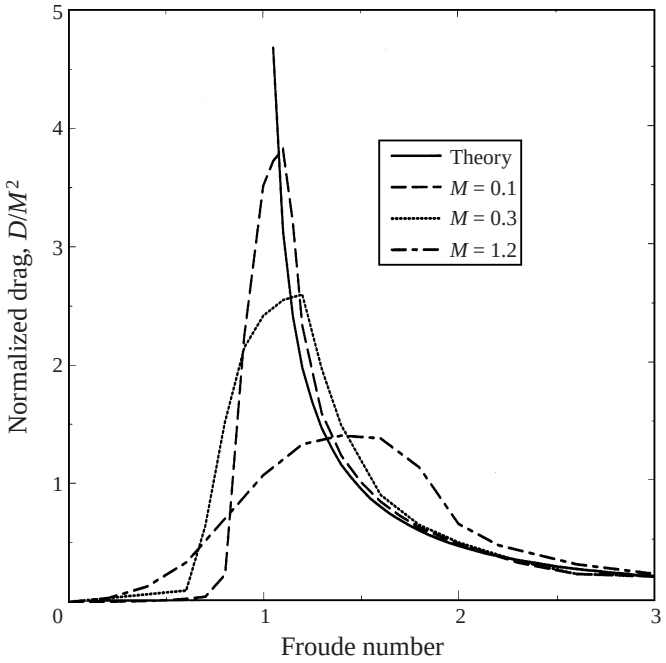

FIGURE 7. Dimensionless (by $\rho g' h_m^2 a$) mountain V-wave drag versus upstream Froude number for fixed mountain heights: $M = 0.1$, 0.3, and 1.2. The solid curve is the linear theory prediction.

With (23), (24), and (26), the V-wave drag can be expressed as

$$D = \mathrm{i}\rho g a^4 \int\int_{-\infty}^{\infty} \frac{(F_\infty^2 - \mathrm{i}\nu k^3/K^2) k h_m^2 \mathrm{e}^{-2aK}}{(F_\infty^2 - K^2 k^{-2} - \mathrm{i}\nu k^3/K^2)} \,\mathrm{d}k\,\mathrm{d}l. \tag{28}$$

Evaluating (28) for small viscosity (see Appendix B), we obtain $D = 0$, for $F_\infty < 1$. That is, linear theory predicts zero drag for subcritical flow (SS93*a*). The flow pattern is fore-aft symmetric relative to the obstacle for subcritical flow over small topography.

For $F_\infty > 1$, (28) gives

$$D = \frac{\pi \rho g' h_m^2 a F_\infty^{-2}}{2\sqrt{1 - F_\infty^{-2}}} \tag{29}$$

or in non-dimensional form (normalized by $\rho g' a H_\infty^2$)

$$\bar{D} = \frac{\pi M^2 F_\infty^{-2}}{2\sqrt{1 - F_\infty^{-2}}}. \tag{30}$$

The numerical solutions with different mountain heights ($M = 0.1$, 0.3, 1.2) normalized by M^2 are plotted on figure 7 as a function of Froude number. Drag (30) normalized by M^2 is represented as a dashed curve for comparison.

For subcritical flow, drag comes from nonlinear transitional flow and hydraulic jumps; therefore, it cannot be predicted by linear theory. For supercritical flow, when M is small, the linear theory prediction shows a good agreement with numerical runs. This agreement becomes poor as M increases.

There is a single-peaked drag structure for all three hill heights with the maximum drag moving to larger Froude number for higher hills (figure 7). Considering that

there is no normal shock present in supercritical ambient flow, this tendency suggests that these two types of drag, the drag due to a normal jump and the V-wave and bow shock drag, are comparable in the transcritical region ($F_\infty \sim 1$). More evidence for this interpretation is given below.

4.2. *Drag law comparisons*

4.2.1. *Comparing with mountain drag on the atmosphere*

Mountain wave drag for continuously stratified flow over obstacles has been discussed previously (e.g. Sawyer 1959; Eliassen & Palm 1960; Blumen 1965; Miles 1969; Bretherton 1969; Smith 1988; and Grubišić & Smolarkiewicz 1997). For instance, for deep hydrostatic flow with zero shear and a constant Brunt–Väisälä frequency N, wave drag on a circular hill of form (10) can be expressed as (Smith 1988)

$$D = \frac{\pi}{4}\rho_0 N U a h_m^2 \tag{31}$$

where U is horizontal velocity, a is the half-width of the mountain, and h_m is the mountain height. The common proportionality to h_m^2 in (29) and (31) is a characteristic of linear theory.

Unlike (31) however, (29) predicts that the drag decreases with increasing flow velocity. Considering the different drag mechanisms for continuously stratified flow and single-layer shallow water flow, this difference is not surprising. In continuously stratified flow, the momentum is transferred vertically (to a level where the wave-breaking occurs) by vertically propagating waves. In shallow water flow, momentum is carried away by the horizontal V-wave. Therefore, as applied to the atmosphere, drag laws (31) and (29) represent the mountain drag on the atmosphere in different limits. While drag law (31) can be generally applied to uniformly stratified flow, drag law (29) can be used to describe mountain drag on a shallow flow layer under a low-level inversion, such as a typical marine boundary layer. The rapid decrease of the V-wave drag with flow speed will be discussed further in § 4.4.

4.2.2. *Comparing with ship drag*

The water waves generated by moving perturbation sources such as ships have been studied extensively. Although forcing produced by a ship is different from that due to underlying topography, it is believed that ship wave theory is relevant to flow past topography, i.e. the two forcings generate similar wake or wave patterns. However, due to the non-hydrostatic effect, for ships in open water, most of the studies focused on deep water dynamics (i.e. $F_\infty \ll 1$). The linear theory for the trim and leak of a shallow water wave on a ship of gentle shape was given by Tuck (1966). The decrease of wave drag with increasing Froude number has been found in supercritical flow. Weakly nonlinear and dispersive ship wave drag has been examined by Mei (1976). A similar single peaked drag function has been identified. However, due to the different forcing sources, it is difficult to compare with these results in a more quantitative manner.

4.3. *Momentum flux and nonlinear V-wave drag*

The drag law (29) can be recovered from the asymptotic linear solution (13) in the following way. Without a wake, the total V-wave drag on the hill should equal the total momentum flux across the two beams. The y-directed flux of x-momentum can

be expressed as

$$D = 2\rho \int_{-\infty}^{\infty} uvH_{\infty}\,\mathrm{d}x \tag{32}$$

where the factor 2 is for the two legs of the V-wave, and perturbation velocity (u, v) can be obtained from linearized momentum equations (5) and (6):

$$u = -g'\eta/U_{\infty}, \tag{33}$$

$$v = g'\frac{B}{A}\eta/U_{\infty}. \tag{34}$$

Combining (32)–(34), we obtain

$$D = \frac{2\rho g'^2 BH_{\infty}}{AU_{\infty}^2}\int_{-\infty}^{\infty}\eta^2(x)\,\mathrm{d}x. \tag{35}$$

or equivalently, in local coordinates

$$D = \frac{2\rho g'^2 BH_{\infty}}{AU_{\infty}^2}\int_{-\infty}^{\infty}\eta^2(\xi)\,\mathrm{d}\xi. \tag{36}$$

Using (36) and the asymptotic solution (13), we obtain

$$D = \frac{\pi\rho g' h_m^2 a F_{\infty}^{-2}}{2\sqrt{1 - F_{\infty}^{-2}}}. \tag{37}$$

Drag law (37) is identical with (29). Notice that from (33) and (34), we get $u \propto \eta/F_{\infty}$ and as $F_{\infty} \gg 1$, $v \propto F_{\infty}\eta$. Therefore, using (36), we get $D \propto \int \eta^2\,\mathrm{d}x$, independent of F_{∞}. However, η, the amplitude of the V-wave, decreases with increasing Froude number (e.g. (13)). Therefore, D decreases as F_{∞} increases.

Using the asymptotic solution (15), the drag for an elliptical hill, $\hat{D}$, can be represented as

$$\hat{D} = \frac{8\rho g' A^2 h_m^2}{cB}\int_{-\infty}^{\infty}\frac{\xi^2}{(1+\xi^2)^4}\,\mathrm{d}\xi \tag{38}$$

or

$$\hat{D} = \frac{\pi\rho g' abA^2 h_m^2}{2(A^2 b + B^2 a)B}. \tag{39}$$

For a circular hill with $a = b$, the drag law (39) reduces to (29) and (37).

Notice, in (39), as $b/a \to \infty$, $\hat{D} \to \pi\rho g' a h_m^2/(2B)$. The fact that $\hat{D}$ approaches a constant as b increases to infinity agrees with the known result that the drag per unit length of an infinite ridge is zero in linear supercritical flow. Physically, for a long ridge, V-wave generation and drag only appears near the two ends of the ridge. The V-wave disturbances from the uniform parts interfere with each other and cancel out.

In the limit of a long and narrow hill oriented with the flow direction ($a/b \to \infty$), we get $\hat{D} \to \pi\rho g' bA^2 h_m^2/(2B^3)$, independent of a. Again, only the ridge ends generate V-waves and drag.

The formula (39) will become inappropriate when the nonlinearity of the V-wave increases. It is not only that the wave shape changes, but also the wavebreaking will generate a wake behind the hill with a momentum deficit. However, the nonlinear N-wave drag contribution can still be estimated by the V-wave momentum flux integral (35).

Assuming that η is a linear function of x across the N-wave, we have $\eta = -2\hat{A}x/L$, for $|x| \leqslant L/2$, where $\hat{A}$ is the amplitude of the N-wave, which is a function of Froude

number and mountain height, and L is the length of the N-wave. Using (35), the momentum flux across the N-wave can be expressed as

$$D_N = \frac{\rho g'^2 H_\infty B \hat{A}^2 L}{3AU_\infty^2} \tag{40}$$

or in non-dimensional form,

$$\bar{D}_N = \frac{B\hat{A}^2 L}{3AF_\infty^2} \tag{41}$$

where $\bar{D}_N = D_N/(\rho g' a H_\infty^2)$, and $\hat{A}$ and L are non-dimensionalized by H_∞ and a, respectively.

Note that both L and $\hat{A}$ can be obtained from numerical solutions. For example, with $F_\infty = 1.5$, $M = 1.2$, the total drag predicted by the numerical model is $\bar{D}_N = 2.03$. Along $y = 5$, we get $\hat{A} = 0.6$, $L = 18.2$. Substituting into (41), we obtain a momentum flux across $y = \pm 5$ of 1.3 non-dimensional units, which means that 65% of total drag is put into the wave, and 35% is put into the wake.

4.4. *Collective behaviour*

The rapid decrease in drag as the Froude number passes unity (figure 7) could give rise to uncontrolled acceleration or a bistable behaviour in flow systems which are forced by a fixed pressure gradient or body force. Such behaviour has been widely discussed in regard to transonic flight, ship design and other fluid dynamical systems with non-monotonic drag curves. In the present case, the occurrence of catastrophic acceleration will depend on what other drag mechanisms exist on the fluid and how the fluid system is constrained. To investigate these issues we parameterize the non-dimensional drag law in figure 7 by

$$\bar{D}(F, M) = CM^\gamma \mathrm{e}^{-((F-\bar{\alpha})/\bar{\beta})^2} \tag{42}$$

where $C = 1.6$, $\gamma = -0.40$, $\bar{\alpha}(M) = 1 + 0.3\sqrt{M}$ and $\bar{\beta}(M) = 0.6\sqrt{M}$. This Gaussian formula (42) approximately describes the height (CM^γ), width ($\bar{\beta}$), and location ($\bar{\alpha}$) of the drag peak.

Now consider a layer of fluid, with a free surface, driven by a horizontal pressure gradient (P_x) and resisted by a combination of a quadratic bottom friction and obstacle drag so that in steady state

$$P_x H = \tfrac{1}{2}\rho U^2 C_d + \rho g h_m^2 a \bar{N} \bar{D}(F, M) \tag{43}$$

where C_d is the bottom friction coefficient, $F = U/\sqrt{gH}$, a is the half-width of the obstacles and $\bar{N}$ is the number density of obstacles on the bottom surface.

If the depth H is kept constant, (43) defines a relationship between the driving pressure gradient and the flow speed: $P_x(U)$ or $U(P_x)$. Dimensional and numerical analysis of (42)–(43) indicates that dual steady states will occur when the parameter $K = h_m a \bar{N}/C_d > 0.75$. Under this condition, the obstacle drag plays a large role relative to bottom friction, and it drops rapidly enough beyond $F = 1$ that uncontrolled acceleration will occur in a small range of slightly supercritical Froude numbers. To apply this result, consider an atmospheric example with $h_m = 500\,\mathrm{m}$, $a = 1000\,\mathrm{m}$, $C_d = 0.01$ and $\bar{N} = 10^{-8}\,\mathrm{m}^{-2}$ (i.e. one obstacle in each 10 km by 10 km square). These values yield $K = 0.5$, just below the critical value (0.75). Higher, broader or more frequent obstacles, or a reduced bottom friction, would increase K and lead to a bistable system.

River flows driven by streambed slope and gravity can be treated in a similar way, but the volume flow rate per unit width $Q = UH$ should be held constant, rather than the depth H. For certain values of the non-dimensional parameters, two steady states exist: a deep slow subcritical state and a shallow fast supercritical state.

5. Bow wave structure and vorticity generation

5.1. *Bernoulli change and vorticity generation*

The irrotational shallow water equations (1)–(3) materially conserve potential vorticity, i.e.

$$\frac{\mathrm{D}q}{\mathrm{D}t} = 0 \tag{44}$$

where q is the potential vorticity defined as

$$q = \boldsymbol{k} \cdot (\nabla \times \boldsymbol{V})/H. \tag{45}$$

For steady state flow, the Bernoulli function is constant along each streamline:

$$\boldsymbol{V} \cdot \nabla B = 0 \tag{46}$$

where B is the Bernoulli function defined as (Batchelor 1967)

$$B = \tfrac{1}{2}\boldsymbol{V} \cdot \boldsymbol{V} + g'(H + h). \tag{47}$$

SS93*a* demonstrated that for inviscid flow, equation (44) and equation (46) can only be violated in a dissipative region such as a hydraulic jump. When a hydraulic jump forms, the inviscid shallow water equations become incomplete. The internal dissipation in the jump region reduces the Bernoulli constant and generates potential vorticity. They called this process *Pseudoinviscid vorticity generation* to distinguish it from explicitly viscous flow. In Schär (1993), SS93*a*, and Smith & Smith (1995), vertical vorticity generation was directly related to the gradient of the Bernoulli function as

$$\zeta = -\frac{1}{U}\frac{\partial B}{\partial n} \tag{48}$$

where U is the magnitude of velocity, ζ is vertically oriented vorticity, and n is the direction normal to the flow velocity.

In the remaining part of this section, the bow shock and V-shock will be analysed in terms of Bernoulli change and vorticity generation.

5.2. *The bow shock*

For supercritical flow, the non-dispersive infinitesimal x-oriented gravity waves generated by the topography are advected downstream. Hence, in a steady state, there is no disturbance found upstream of the obstacle until a finite-amplitude hydraulic jump forms. The finite-amplitude waves with a larger wave speed can balance the supercritical flow, and therefore, a stationary bow shock can maintain itself upstream of the topography. Here we treat the bow shock in front of a two-dimensional bump as a curved hydraulic jump (figure 8).

If the curvature is not too large, we can assume that the tangential component (along the jump) of velocity is continuous, while in the direction normal to the jump, the one-dimensional jump condition is applicable to each short 'segment':

$$U_n H = U_n' H', \tag{49}$$

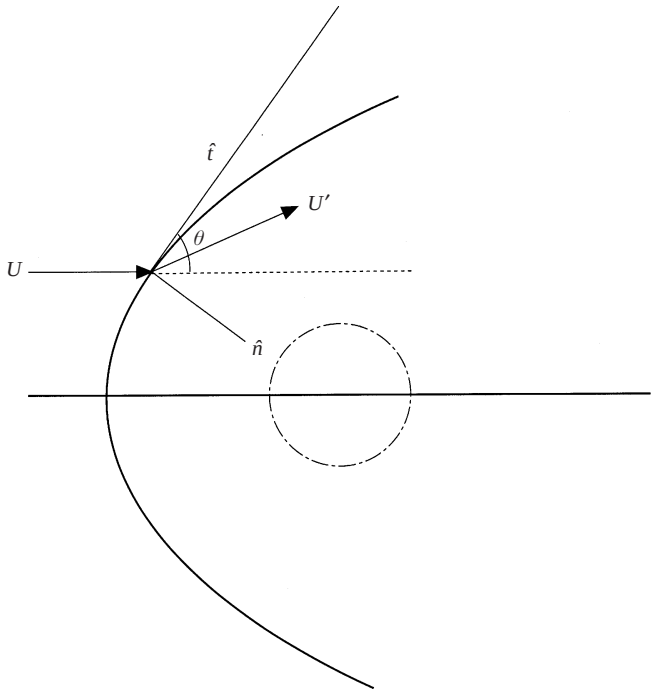

FIGURE 8. Notation sketch of a bow wave jump. U is the incoming flow, $\hat{t}$ is the local orientation of the jump, and $\hat{n}$ represents the normal direction.

$$HU_n^2 + \tfrac{1}{2}g'H^2 = H'U_n'^2 + \tfrac{1}{2}g'H'^2, \tag{50}$$

where H is flow depth upstream of the jump, $U_n = U\sin\theta$ is the upstream velocity component normal to the jump, H' and U_n' are the corresponding quantities downstream of the jump, and θ is the angle between the flow and the local orientation of the jump (figure 8). The downstream state can be expressed in terms of the upstream Froude number ($F = U/\sqrt{g'H}$) and the inclination angle θ (Baines 1995, pp. 79–80):

$$\frac{H'}{H} = \tfrac{1}{2}(G-1) \tag{51}$$

where

$$G = (1 + 8F^2\sin^2\theta)^{1/2} \tag{52}$$

and $\theta > \alpha_0$, where α_0 is the Mach angle. Near the centreline, $\theta = \pi/2$, and equation (51) and equation (52) reduce to

$$2F^2 = \frac{H'}{H}\left(1 + \frac{H'}{H}\right) \tag{53}$$

which is the normal shock condition.

The Froude number immediately downstream of the normal jump can be expressed as:

$$F' = F\left(\frac{H}{H'}\right)^{3/2} = \frac{(\sqrt{1+8F^2}+1)^{3/2}}{8F^2}. \tag{54}$$

For $F > 1$, it is easy to show that $F' < 1$. Hence to have a stationary bow shock, the

flow near the centreline must experience a state transition from supercritical flow to subcritical flow.

5.3. *Vorticity generation*

Immediately after a curved jump like a bow shock, the vorticity generated by dissipation can be expressed as (Baines 1995)

$$\zeta = Uk\cos\theta\left(1+\frac{1+G}{4GF^2\sin^2\theta}\right) \tag{55}$$

where θ is the inclination angle, G is defined in (52), and k is the curvature of the shock. Formula (55) shows how the vorticity behind the shock varies with Froude number and the shock shape. At the normal position ($\theta = \pi/2$), $\cos\theta$ vanishes and so does the vorticity. Far away from the centreline, θ approaches the Mach angle. Therefore, the curvature vanishes, and again, the vorticity vanishes.

As an example, consider a hyperbolic-shaped shock given by (Rasmussen 1994, p. 39),

$$y_s = \sqrt{2Rx_s + x_s^2/(F^2-1)}. \tag{56}$$

Here (x_s, y_s) are local coordinates with the origin $(0,0)$ at the nose of the shock and R is the radius of the shock near $y_s = 0$. As $x_s \to \infty$, (56) reduces to $y_s/x_s = 1/\sqrt{F^2-1}$, which is the Mach angle.

Using (56) to determine k in (55), the normalized (by R/U) vorticity can be expressed as a function of F and the inclination angle θ. Figure 9 shows the vorticity generated by these types of shocks with different upstream Froude numbers and at various inclination angles. Obviously, as F increases, while the maximum scaled vorticity only varies slightly (between 0.3 and 0.4), the position of maximum vorticity moves away from the centreline ($y = 0$), and the vorticity region becomes wider.

Notice that for our idealized bell-shaped hill, R can only be a function of upstream Froude number and hill height (i.e. F_∞ and M). For instance, from numerical runs, $R = 28$ for $F_\infty = 1.2$, $M = 1.0$, $R = 14$ for $F_\infty = 1.4$, $M = 2.2$, and $R = 7.8$ for $F_\infty = 1.6$, $M = 1.0$. Therefore, we can estimate that the maximum vorticity from figure 9, will be approximately 0.04, 0.11, and 0.19, respectively. Although these values are small, the numerical solutions suggests that R decreases rapidly with increasing Froude number, and R is not very sensitive to hill height. Thus, for hypercritical flow ($F_\infty \gg 1$), strong wake vorticity could be generated by a highly curved bow shock.

The weak vorticity generation found for moderately supercritical Froude numbers implies that the wake will be absolutely stable and no eddy shedding will occur (Schär & Smith 1993*b*).

5.4. *Oblique shocks and V-wave breaking*

Assume now that apart from the centreline, each leg of the trailing wave can be treated as an oblique shock, satisfying (51) and (52). For a V-wave shock with a Mach angle, i.e. $\alpha_0 = \arcsin(Fr_\infty^{-1})$, (51) and (52) predict $H'/H = 1$, i.e. a linear V-wave without discontinuity. If the V-wave has a small departure from the Mach angle, i.e.

$$\theta = \alpha_0 + \varepsilon \tag{57}$$

and $\varepsilon \ll 1$, to the first order of ε, we have, using (51)

$$\frac{H'}{H} = 1 + \tfrac{4}{3}\varepsilon\sqrt{F^2-1}. \tag{58}$$

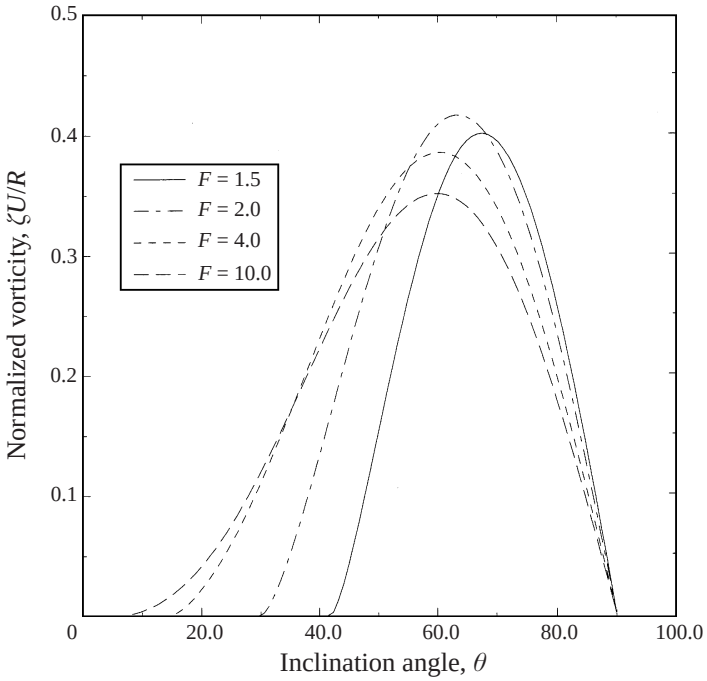

FIGURE 9. Vorticity generation after a bow shock assuming a hyperbolic shape (56). Vorticity is scaled with R/U.

Using (47) and (58), Bernoulli change will be,

$$\delta B = -\tfrac{4}{3} H\varepsilon(F^2 - 1)^{3/2}. \tag{59}$$

After a dissipative jump, $\delta B < 0$, therefore $\varepsilon > 0$, suggesting that nonlinear V-wave can only be maintained at an angle larger than the Mach angle. Compared with a normal shock, the Bernoulli loss after an oblique shock is $O(\varepsilon)$ smaller.

The deflection angle across the oblique jump can be derived from the jump condition (51):

$$\tan\theta' = \frac{\tan\theta(G-3)}{G-1+2\tan^2\theta}. \tag{60}$$

Notice that $G > 3$ in (52), therefore θ' has the same sign as θ, which means that after a finite bow shock or a V-shock, the flow is always deflected away from the centreline.

The uppermost supercritical regime in figure 3 is characterized by flow splitting around the obstacle and a dry zone where the flow depth $H = 0$. We have shown that the centre part of the upstream bow shock is equivalent to a normal shock with state transition. However, no state transition has been found after a V-wave shock even in high-resolution ($DX = DY = 0.05$) simulations. This suggests that there is no normal shock at the intersection point of the left and right V-wave shocks.

On the upstream side, the centre streamline decelerates to a stagnation point (s) (figure 10). If the depth and speed decrease linearly to zero at this point the Froude number will approach zero and thus remain subcritical. The lateral flow along the split streamline immediately becomes supercritical after leaving s, as the depth is small (or zero).

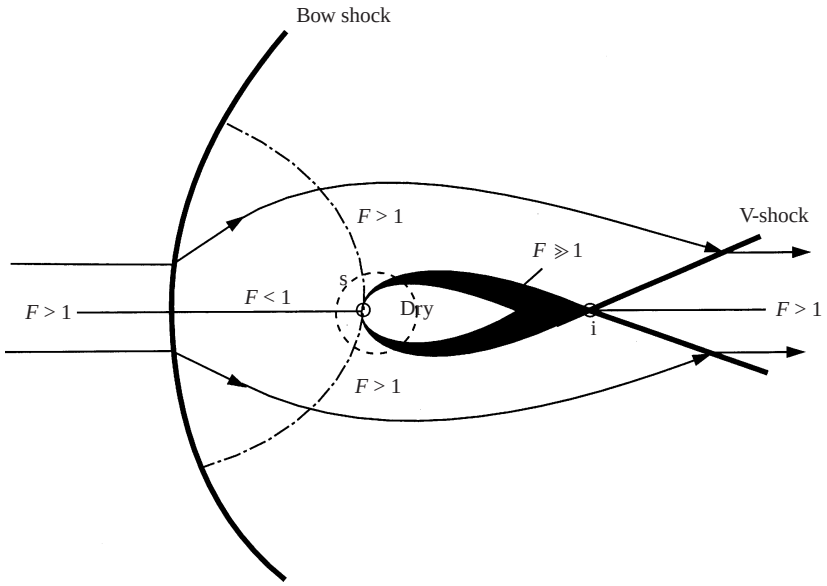

FIGURE 10. Schematic structure of flow splitting and the V-wave for high obstacles in supercritical flow. The dark region represents hypercritical flow ($F \gg 1$) as the fluid depth approaches zero near the dry zone.

As the flow accelerates laterally away from the stagnation point s, the height of the split streamline drops according to Bernoulli's law (46)–(47):

$$\tfrac{1}{2}\rho u^2 + \rho g z = B_c < B_\infty. \tag{61}$$

As the split streamline passes around the obstacle, it continues to drop in altitude and the fluid speed increases.

The downstream end of the dry zone has an intersecting point i. As this point occurs at a lower altitude than the upstream stagnation point s, its velocity must be non-zero. Therefore, from (46) and (47), it is not a stagnation point. Supercritical flow converges toward the centreline and, in the vicinity of i, is shocked into a x-axis-parallel flow by a finite-amplitude V-jump. Thus the point i is singular as it is the intersection of the dry zone, two converging supercritical streams, two V-jumps, and a region of finite-depth axis-parallel supercritical flow.

A similar lee-side V-shock intersection is found in the middle supercritical regime (figure 3). Unlike the dry case however, a centreline flow which passed over the obstacle approaches the intersection (figure 5). Our numerical solutions show no evidence of subcritical flow downstream of the intersection and thus no support for the existence of a normal shock. There is however a Bernoulli drop along the centreline across the V-shock intersection. Consider this example. For $F_\infty = 1.4$, $M = 1.0$, we take two sections ($x = \text{const}$) immediately after the bow shock and V-shock respectively; the normalized (by the upstream value) Bernoulli function is plotted as a function of cross-stream distance (figure 11). A subcritical case ($F = 0.8$, $M = 0.6$) is also plotted for comparison. For this special case, the V-wave shock introduces larger Bernoulli loss than the bow shock does, and concentrated in a smaller region around the centreline. In fact, the width of the loss zone is barely resolved on our grid. The distribution of Bernoulli loss after a V-wave suggests that there may be a finite-amplitude shock at the intersection point of the left and right V-waves. If the

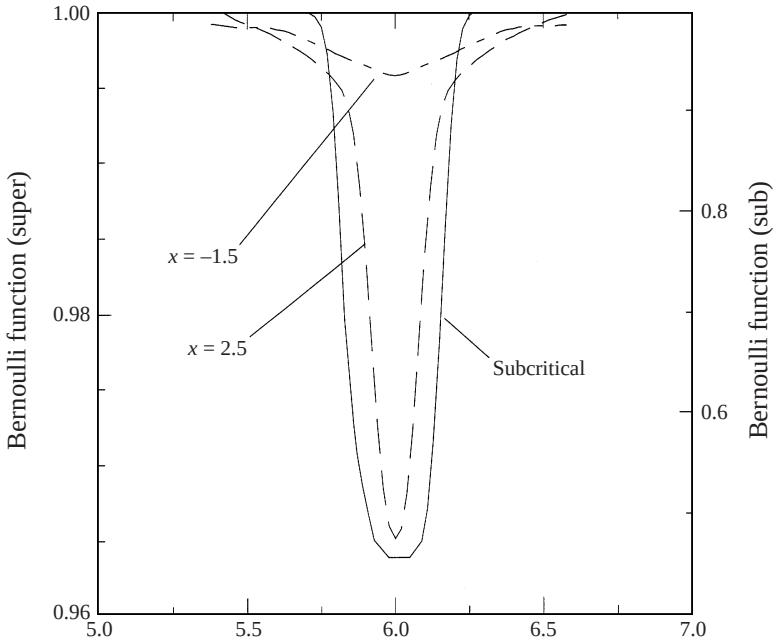

FIGURE 11. Cross-section plot of normalized (by their appropriate far upstream values) Bernoulli function for $F_\infty = 1.4$, $M = 1.0$, at $x = -1.5$ (after the bow shock), and $x = 2.5$ (after the V-wave shock). The solid curve is the same quantity (with a different scale) after a normal jump for subcritical flow: $F_\infty = 0.5$, $M = 0.6$, $x = 2.5$. Cross-stream gradients in B are related to vertical vorticity according to (48).

incoming flow in front of the V-wave is parallel, a finite V-wave shock would induce finite deflection away from the centreline. The centre streamline will split and a dry wedge will appear downstream of the V-wave (e.g. Liepmann & Roshko 1967). This has not been observed. Therefore, if the shocks at the intersection are finite, the incoming flow cannot be parallel, and must have a non-zero component towards the centreline. The straightness of the V-shock (figure 5) is due to a cancellation of two lateral gradients in the approaching flow along the shock: decreasing Froude number and increasing velocity component toward the centreline. Downstream of the V-shock intersection, the flow appears to be parallel and uniform.

6. Conclusions

The structure and behaviour of both linear and nonlinear waves, and related drag and vorticity generation, are investigated within the framework of free surface shallow water flow over an isolated hill. In the absence of bottom friction and ambient rotation, there are only two controlling parameters for this system: upstream Froude number F_∞ and non-dimensional hill height M.

As F_∞ approaches 1, the drag increases rapidly due to nonlinear transcritical flow. A lee-slope normal jump creates a strong wake with large Bernoulli deficit and vorticity generation. As F_∞ increases past 1, the drag is still high, perhaps even higher; however, the drag is due to the nonlinear V-waves. The lee-slope normal jump disappears. Numerical runs show that the contribution from the momentum deficit in the wake and from the transport of momentum out of the domain by V-waves are of

the same order. The bow shocks and oblique lee shocks, if present, generate a broad but weak wake with little vorticity generation. No eddy shedding is seen.

For high hills, with 'dry' peaks, the flank shocks disappear when $F_\infty > 1$. This is so because not only the shallow edge flow, but also the deeper environment, is supercritical. The existence of a bow shock does not make the local environment of the hill subcritical. The shocked subcritical flow is quickly brought back to supercritical by turning around the obstacle.

When F_∞ increases further, the drag drops rapidly and the contribution from the momentum deficit in the wake vanishes. The drag is well represented by the linear theory of V-waves. A closed form expression is derived for both V-wave structure and drag for a circular hill, and further generalized to include a family of elliptical hills. The rapid decrease in drag in low supercritical conditions can cause run-away accelerations or bi-state behaviour in momentum forced systems.

As F_∞ increases to 2 and beyond, moderately high obstacles shift into the submerged regime and eventually into the regime with no bow shocks. The V-waves become very oblique, trailing almost like a wake.

For high obstacles, increasing F_∞ causes the bow shock to become stronger and more curved. Under these conditions, the bow shock can generate significant wake vorticity.

These results can be applied to atmospheric flows, as well as river and coastal flow with bottom topography, when the assumptions of our analysis are satisfied. Several of our results could be tested in laboratory flume experiments, with care taken to keep the flow in the hydrostatic regime.

Christoph Schär kindly allowed us to use his shallow water code. This research was supported by the National Science Foundation, Division of Atmospheric Sciences (ATM-9711076)

Appendix A. The derivation of solution (9)

The Green's function for equation (8) for an infinite domain can be expressed as (Morse & Feshbach 1953, p. 843):

$$G(x, y \mid x_0, y_0) = 2\pi\sqrt{F_\infty^2 - 1}[1 - w(\sqrt{F_\infty^2 - 1}|y - y_0| - (x - x_0)] \qquad \text{(A 1)}$$

where $w(z) = 1$ when $z \geqslant 0$, otherwise $w(z) = 0$. Equation (A 1) suggests that each point source has a uniform influence on the downstream domain within the Mach angle.

The solution of (8) can be expressed as (Morse and Feshbach, 1953)

$$\eta(x, y) = \frac{F_\infty^2}{4\pi\sqrt{F_\infty^2 - 1}} \int_{-\infty}^{\infty} \int_{-\infty}^{\infty} G(x, y \mid x_0, y_0) h_{xx}(x_0, y_0)\, \mathrm{d}x_0\, \mathrm{d}y_0. \qquad \text{(A 2)}$$

Consider the influence of a point source (x_0, y_0) on a field point (x, y). For a fixed y_0, if $y_0 > y$, the point source has influence (i.e. $G(x, y \mid x_0, y_0) = 2\pi\sqrt{F_\infty^2 - 1}$) on (x, y), only when $-\infty < x_0 < x + \sqrt{F_\infty^2 - 1}(y - y_0)$. Otherwise this source has no influence (i.e. $G(x, y \mid x_0, y_0) = 0$) on (x, y). Similarly, for a fixed y_0, if $y_0 < y$, the point source has influence on (x, y), only when $-\infty < x_0 < x - \sqrt{F_\infty^2 - 1}(y - y_0)$. Otherwise this source has no influence on (x, y).

Therefore, (A 2) can be expressed as

$$\eta(x,y)=\frac{1}{2}\int_{-\infty}^{y}\mathrm{d}y_0\int_{-\infty}^{x-\sqrt{F_\infty^2-1}(y-y_0)}h_{xx}(x_0,y_0)\,\mathrm{d}x_0 +\frac{1}{2}\int_{y}^{\infty}\mathrm{d}y_0\int_{-\infty}^{x+\sqrt{F_\infty^2-1}(y-y_0)}h_{xx}(x_0,y_0)\,\mathrm{d}x_0. \tag{A 3}$$

Using $h_x(-\infty,y_0)=0$, we get the solution to (8):

$$\eta(x,y)=\frac{F_\infty^2}{\sqrt{F_\infty^2-1}}\frac{\partial}{\partial x}\left\{\int_{-\infty}^{y}h(x+\sqrt{F_\infty^2-1}(y-y_0),y_0)\,\mathrm{d}y_0 +\int_{y}^{\infty}h(x-\sqrt{F_\infty^2-1}(y-y_0),y_0)\,\mathrm{d}y_0\right\}. \tag{A 4}$$

Substituting the elliptical hill (14) into (A 4), we obtain

$$\begin{aligned}\eta(x,y)=&-\frac{AM}{B}\left\{\frac{Ax/a-By/b}{[1+(Ax/a-By/b)^2]^2}+\frac{Ax/a+By/b}{[1+(Ax/a+By/b)^2]^2}\right\}\\ &-\frac{Mx/a}{2B(1+R^2)^{3/2}}\left\{\frac{Bx/a-Ay/b}{1+(Ax/a+By/b)^2}+\frac{Bx/a+Ay/b}{1+(Ax/a-By/b)^2}\right\}\\ &+\frac{M}{2(1+R^2)^{1/2}}\left\{\frac{1}{(1+(Ax/a+By/b)^2)^2}+\frac{1}{(1+(Ax/a-By/b)^2)^2}\right\}\\ &+\frac{M}{2B(1+R^2)^{1/2}}\left\{\frac{(Ax/a+By/b)(-ABx/a+B^2y/b+2A^2y/b)}{[1+(Ax/a+By/b)^2]^2}\right.\\ &\left.+\frac{(By/b-Ax/a)(ABx/a+B^2y/b+2A^2y/b)}{[1+(Ax/a-By/b)^2]^2}\right\}.\end{aligned} \tag{A 5}$$

Here $R^2=(x/a)^2+(y/b)^2$, and A,B are defined in § 2.

Appendix B. Contour integration of (28)

Using the following transformation: $k=K\cos\theta$, $l=K\sin\theta$, integral (28) can be expressed in cylindrical coordinates (K,ψ) as

$$D=\mathrm{i}\rho g a^4\left(\int_0^\infty\int_0^{2\pi}\frac{F_\infty^2K^2\cos^2\theta}{F_\infty^2\cos^2\theta-1-\mathrm{i}\nu K\cos^3\theta}\mathrm{e}^{-2aK}\,\mathrm{d}\theta\,\mathrm{d}K -\int\int_{-\infty}^{\infty}\frac{\mathrm{i}\nu K^3\cos\theta\mathrm{e}^{-2aK}}{F_\infty^2\cos^2\theta-1-\mathrm{i}\nu K\cos^3\theta}\mathrm{e}^{-2aK}\,\mathrm{d}\theta\,\mathrm{d}K\right). \tag{B 1}$$

For small friction ($\nu\ll 1$), the contribution of the second term is negligible. Considering $\mathrm{e}^{-2aK}\to 0$, as $K\to\infty$, the integral can be approximated by $\int_0^{K_c}\mathrm{d}K$, where $K_c>0$ is certain finite value. Therefore, the quantity $\nu K\cos^2\theta$ is positive but can be arbitrarily small, hence, we can replace this term by a small quantity ε; $0<\varepsilon\ll 1$.

Integral (B 1) becomes

$$D=\mathrm{i}\rho g a^4\int_0^\infty K^2\mathrm{e}^{-2aK}\,\mathrm{d}K\int_0^{2\pi}\frac{F_\infty^2\cos^3\theta}{F_\infty^2\cos^2\theta-1-\mathrm{i}\varepsilon\cos\theta}\,\mathrm{d}\theta \tag{B 2}$$

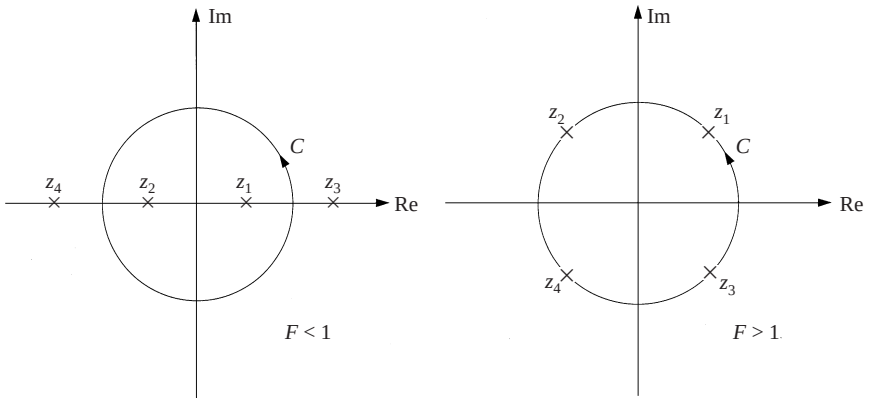

FIGURE 12. Sketch of contour integral for linear theory drag. Symbols × represent singular points.

or

$$D = \frac{\mathrm{i}}{4}\rho g a h_m^2 I \tag{B 3}$$

where

$$I = \int_0^{2\pi} \frac{F_\infty^2 \cos^3\theta}{F_\infty^2 \cos^2\theta - 1 - \mathrm{i}\varepsilon\cos\theta}\,\mathrm{d}\theta. \tag{B 4}$$

To use contour integration, we transform the integral variable: $z = \mathrm{e}^{\mathrm{i}\theta}$, so that

$$I = \oint \frac{\mathrm{d}z}{2\mathrm{i}z^2} \frac{(z^2+1)^3}{(z^2+1)^2 - 2\mathrm{i}z\varepsilon(z^2+1) - F_\infty^{-2}(2z)^2}. \tag{B 5}$$

The integrand in (B 5) has five poles:

$$z_{1\sim4} = 0.5\mathrm{i}\varepsilon \mp F_\infty^{-1} \pm \sqrt{F_\infty^{-2} - 1}, \tag{B 6}$$

$$z_5 = 0; \tag{B 7}$$

z_1–z_4 are simple poles and z_5 is a pole of second order. For $F_\infty < 1$, the distribution of these poles are as figure 12. Therefore,

$$I = 2\pi\mathrm{i}(\mathrm{res}\,(z_3) + \mathrm{res}\,(z_4) + \mathrm{res}\,(z_5)). \tag{B 8}$$

Evaluating these residues at $\varepsilon \to 0$, we get

$$D = 0 \tag{B 9}$$

for $F_\infty < 1$. For $F_\infty > 1$, the distribution of these poles is schematically plotted on figure 12.

Notice with $\varepsilon = 0$, z_1–z_4 are on the unit circle and symmetric relative to the centre of the circle, and the sum of the four residues is zero. With $\varepsilon > 0$ (positively defined viscosity), z_3 and z_4 move into the circle, and z_1 and z_2 move out of the circle. Physically, z_3 and z_4 represent the contribution of the two legs of the downstream V-wave poles; z_1 and z_2 represent the contribution of the two legs of the upstream V-wave, which is removed by the introduction of small friction.

Notice that for $\varepsilon \to 0$, $z_1 \sim z_4$ can be rewritten as

$$z_1 = \mathrm{e}^{\mathrm{i}(\pi/2-\alpha_0)}, \quad z_2 = \mathrm{e}^{\mathrm{i}(\pi/2+\alpha_0)}, \quad z_3 = \mathrm{e}^{\mathrm{i}(3\pi/2-\alpha_0)}, \quad z_4 = \mathrm{e}^{\mathrm{i}(3\pi/2+\alpha_0)}. \tag{B 10}$$

Using (B 10), we have

$$\mathrm{res}\,(z_5) = \frac{\mathrm{d}}{\mathrm{d}z}\left(\frac{(z^2+1)^3}{2\mathrm{i}((z^2+1)^2 - F_\infty^{-2}(2z)^2)}\right)\bigg|_{z=0} = 0, \tag{B 11}$$

$$\mathrm{res}\,(z_3) = \mathrm{res}\,(z_4) = -\frac{\sin^2\alpha_0}{2\cos\alpha_0}. \tag{B 12}$$

Substituting (B 11) and (B 12) into (B 8), we get

$$I = -2\pi\mathrm{i}\frac{\sin^2\alpha_0}{\cos\alpha_0}. \tag{B 13}$$

Finally we get the formula for V-wave mountain drag:

$$D = \frac{\pi\rho g h_m^2 a F_\infty^{-2}}{2\sqrt{1-F_\infty^{-2}}}. \tag{B 14}$$

REFERENCES

Baines, P. G. 1995 *Topographic Effects in Stratified Flows*. Cambridge University Press.

Batchelor, G. K. 1967 *An Introduction to Fluid Dynamics*. Cambridge University Press, London.

Binnie, A. M. & Orkney, J. C. 1955: Experiments on the flow of water from a reservoir through an open horizontal channel. II. The formation of hydraulic jumps. *Proc. R. Soc. Lond.* A **230**, 237–246.

Blumen, W. 1965 A random model of momentum flux by mountain waves. *Geofys. Publ.* **26**, 1–33.

Bona, J. L., Prichard, W. G. & Scott, R. L. 1981 An evaluation of a model equation for water waves. *Phil. Trans. R. Soc. Lond.* **302**, 457–510.

Bretherton, F. P. 1969 Momentum transport by gravity waves. *Q. J. R. Met. Soc.* **95**, 213–243.

Broad, A. S. 1997 New shallow flows over an obstacle. *Q. J. Mech. Appl. Maths* **50**, 625–653.

Davies, H. C. 1983 Limitations of some common lateral boundary schemes in regional NWP models. *Mon. Wea. Rev.* **111**, 1002–1012.

Eliassen, A. & Palm, E. 1960 On the transfer of energy in stationary mountain waves. *Geofys. Publ.* **22**, 1–23.

Gjevik, B. J. & Marthinsen, T. 1978 Three-dimensional lee wave pattern. *Q. J. R. Met. Soc.* **104**, 947–957.

Grubišić, V., Smith, R. B. & Schär, C. 1995 The effect of bottom friction on shallow-water flow past an isolated obstacle. *J. Atmos. Sci.* **52**, 1985–2005.

Grubišić, V. & Smolarkiewicz, P. K. 1997 The effect of critical levels on 3D orographic flows: Linear Regime. *J. Atmos. Sci.* **54**, 1943–1960.

Haynes, P. H. & McIntyre, M. E. 1987 On the evolution of vorticity and potential vorticity in the presence of diabatic heating and fractional or other forces. *J. Atmos. Sci.* **44**, 828–841.

Houghton, D. D. C. & Kasahara, A. 1968 Nonlinear shallow fluid flow over an isolated ridge. *Commun. Pure Appl. Maths* **21**, 1–23.

Joseph, R. I. 1977 Solitary waves in a finite depth fluid. *J. Phys.* A: *Math. Gen.* **10**, L225–227.

Liepman, H. & Roshko, A. 1967 *Elements of Gasdynamics*. Wiley.

Long, R. R. 1954 Some respects of the flow of stratified fluids, II. Experiments with a two-fluid system. *Tellus* **6**, 97–115.

Long, R. R. 1970 Blocking effects in flow over obstacles. *Tellus* **22**, 471–480.

Kubota, T., Ko, D. R. S. & Dobbs, L. 1978 Weakly non-linear, long internal gravity waves in fluids of finite depth. *AIAA J. Hydronaut.* **12**, 157–165.

Mei, C. C. 1976 Flow around a thin body moving in shallow water. *J. Fluid Mech.* **77**, 737–751.

Mei, C. C. 1989 *The Applied Dynamics of Ocean Surface Waves*. World Scientific.

Miles, J. W. 1969 Waves and wave drag in stratified flows. *Proc. 21st Intl Congr. Appl. Mech., 1968*. Springer.

Morse, P. M. & Feshbach, H. 1953 *Methods of Theoretical Physics*, Parts I & II. McGraw-Hill.

PAN, F. & SMITH, R. 1999 Gap winds and wakes: SAR observations and numerical simulations. *J. Atmos. Sci.* **56**, 905–923.

PEREGRINE, D. H. 1968 Long waves in a uniform channel of arbitrary cross-section. *J. Fluid Mech.* **32**, 353–365.

QUENEY, P. 1947 The theory of perturbations in stratified currents with applications to air flow over mountain barriers. *Dept of Meteorology of the Univ. of Chicago, Misc. Rep.* 23.

RASMUSSEN, M. L. 1994 *Hypersonic Flow*. Wiley.

SAMELSON, R. 1992 Supercritical marine-layer flow along a smoothly varying coastline. *J. Atmos. Sci.* **49**, 1571–1584.

SAMELSON, R. & LENTZ, S. 1994 The horizontal momentum balance in the marine atmospheric boundary layer during CODE-2. *J. Atmos. Sci.* **51**, 3745–3757.

SAWYER, J. S. 1959 The introduction of the effects of topography into mehtods of numerical forecasting. *Q. J. R. Met. Soc.* **85**, 31–43.

SCHÄR, C. 1993 A Generalization of Bernoulli's theorem. *J. Atmos. Sci.* **50**, 1437–1443.

SCHÄR, C. & DURRAN, D. R. 1997 Vortex formation and vortex shedding in continuously stratified flows past isolated topography. *J. Atmos. Sci.* **54**, 534–554.

SCHÄR, C. & SMITH, R. B. 1993*a* Shallow-water flow past an isolated topography. Part I: Vorticity production and wake formation. *J. Atmos. Sci.* **50**, 1373–1400 (referred to herein as SS93*a*).

SCHÄR, C. & SMITH, R. B. 1993*b* Shallow-water flow past an isolated topography. Part II: Transition to vortex shedding. *J. Atmos. Sci.* **50**, 1401–1412.

SCHÄR, C. & SMOLARKIEWICZ, P. K. 1996 A synchronous and iterative flux-correction formalism for coupled transport equations. *J. Comput Phys.* **128**, 101–120.

SMITH, R. B. 1979 The influence of mountains on the atmosphere. *Adv. Geophys.* **21**, 87–217.

SMITH, R. B. 1980 Linear theory of stratified hydrostatic flow past an isolated mountain. *Tellus* **32**, 348–364.

SMITH, R. B. 1988 Linear theory of stratified hydrostatic flow over an isolated mountain in isosteric coordinates. *J. Atmos. Sci.* **45**, 3889–3896.

SMITH, R. B. 1989 Hydrostatic airflow over mountains. *Adv. Geophys.* **31**, 1–41.

SMITH, R. B., GLEASON, A. C., GLUHOSKY, P. A. & GRUBIŠIĆ, V. 1997 The wake of St. Vincent. *J. Atmos. Sci.* **54**, 606–623.

SMITH, R. B. & SMITH, D. F. 1995 Pseudoviscid wake formation by mountains in shallow water flow with a drifting vortex. *J. Atmos. Sci.* **52**, 436–454.

STOKER, J. J. 1957 *Water Waves*. Interscience.

WHITHAM, G. B. 1974 *Linear and Nonlinear Waves*. Wiley.

TUCK, E. O. 1966 Shallow-water flows past slender bodies. *J. Fluid Mech.* **26**, 81–95.

WILSON, R. E. 1976 Gravitational circulation in Long Island Sound. Oceanographic Abstract and Bibliography, Oxford, 24, 81.

WU, T. Y. 1987 Generation of upstream advancing solitons by moving disturbances. *J. Fluid Mech.* **184**, 75–99.

WURTELE , M. 1957 The three-dimensional lee wave. *Beitr. Phys. Frei. Atmos.* **29**, 242–252.